Neuron

Autism-Associated Shank3 Is Essential for Homeostatic Compensation in Rodent V1

Highlights

- Shank3 loss blocks synaptic and intrinsic homeostatic plasticity
- Li treatment rescues homeostatic plasticity after Shank3 loss
- Shank3 KO impairs homeostatic compensation to sensory deprivation
- Li rescues an overgrooming phenotype in Shank3 KO mice

Authors

Vedakumar Tatavarty, Alejandro Torrado Pacheco, Chelsea Groves Kuhnle, ..., Florence F. Wagner, Stephen D. Van Hooser, Gina G. Turrigiano

Correspondence

turrigiano@brandeis.edu

In Brief

Shank3 loss or disfunction is strongly associated with autism spectrum disorders. Tatavarty et al. show that Shank3 loss impairs homeostatic plasticity and blocks homeostatic compensation during sensory perturbations; Li treatment restores homeostatic plasticity and normalizes a repetitive behavior. Thus, Shank3 loss impairs homeostatic compensation and renders central circuits vulnerable to perturbations during postnatal development.

Tatavarty et al., 2020, Neuron *106*, 769–777
June 3, 2020
https://doi.org/10.1016/j.neuron.2020.02.033

CellPress

Neuron

CellPress

Report

Autism-Associated Shank3 Is Essential for Homeostatic Compensation in Rodent V1

Vedakumar Tatavarty,[1,3] Alejandro Torrado Pacheco,[1] Chelsea Groves Kuhnle,[1] Heather Lin,[1,4] Priya Koundinya,[1] Nathaniel J. Miska,[1,6] Keith B. Hengen,[1,5] Florence F. Wagner,[2] Stephen D. Van Hooser,[1] and Gina G. Turrigiano[1,7,*]

[1]Department of Biology, Brandeis University, Waltham, MA 02493, USA

[2]Stanley Center for Psychiatric Research, Broad Institute of Massachusetts Institute of Technology and Harvard University, Cambridge, MA, USA

[3]Present address: Kintai Therapeutics, 26 Landsdowne St., Suite 450, Cambridge, MA, USA

[4]Present address: Emory University Medical School, Atlanta, GA, USA

[5]Present address: Department of Biology, Washington University, St. Louis, MO, USA

[6]Present address: Sainsbury Welcome Center, University College London, London, UK

[7]Lead Contact

*Correspondence: turrigiano@brandeis.edu

https://doi.org/10.1016/j.neuron.2020.02.033

SUMMARY

Mutations in Shank3 are strongly associated with autism spectrum disorders and neural circuit changes in several brain areas, but the cellular mechanisms that underlie these defects are not understood. Homeostatic forms of plasticity allow central circuits to maintain stable function during experience-dependent development, leading us to ask whether loss of Shank3 might impair homeostatic plasticity and circuit-level compensation to perturbations. We found that Shank3 loss *in vitro* abolished synaptic scaling and intrinsic homeostatic plasticity, deficits that could be rescued by treatment with lithium. Further, Shank3 knockout severely compromised the *in vivo* ability of visual cortical circuits to recover from perturbations to sensory drive. Finally, lithium treatment ameliorated a repetitive self-grooming phenotype in Shank3 knockout mice. These findings demonstrate that Shank3 loss severely impairs the ability of central circuits to harness homeostatic mechanisms to compensate for perturbations in drive, which, in turn, may render them more vulnerable to such perturbations.

INTRODUCTION

Mutations in the multidomain scaffold protein Shank3 are associated with autism spectrum disorders (ASDs), Phelan-McDermid syndrome, and intellectual disability (Betancur and Buxbaum, 2013). Animal models of Shank3 loss have revealed circuit defects in many brain regions that might contribute to these shankopathies (Bariselli et al., 2016; Bey et al., 2018; Bozdagi et al., 2010; Duffney et al., 2015; Geramita and Urban, 2016; Jaramillo et al., 2017; Kouser et al., 2013; Lee et al., 2015; Orefice et al., 2016; Peça et al., 2011; Peixoto et al., 2016; Schmeisser et al., 2012; Speed et al., 2015; Wang et al., 2011; Yang et al., 2012; Zhou et al., 2019), but a unified view of how Shank3 loss disrupts circuit function is lacking. A common feature of several monogenic ASD rodent models is loss of cellular homeostatic plasticity mechanisms (Blackman et al., 2012; Bulow et al., 2019; Dani et al., 2005; Nelson and Valakh, 2015; Soden and Chen, 2010; Zhong et al., 2018), leading us to ask whether Shank3 loss compromises homeostatic compensation.

Maintenance of circuit stability in the neocortex is achieved through a set of homeostatic plasticity mechanisms, including synaptic scaling (Turrigiano et al., 1998) and intrinsic homeostatic plasticity (Desai et al., 1999), that cooperate to stabilize neuronal firing following perturbations in drive (Hengen et al., 2013; Lambo and Turrigiano, 2013; Hengen et al., 2016). Synaptic scaling bidirectionally scales all excitatory postsynaptic strengths up or down in the right direction to compensate for prolonged perturbations in firing (Turrigiano et al., 1998), whereas intrinsic homeostatic plasticity adjusts the input-output function of neurons by regulating the balance of inward and outward voltage-dependent conductances (Desai et al., 1999; Hengen et al., 2013; Joseph and Turrigiano, 2017). Recent experiments in the rodent primary visual cortex (V1) indicate that perturbing firing through monocular eyelid suture (monocular deprivation [MD]) induces both types of homeostatic plasticity, which then cooperate to restore neuronal firing back to an individual firing rate set point (firing rate homeostasis [FRH]) in the monocular V1 (V1m) and restore net drive from the two eyes during ocular dominance (OD) plasticity in the binocular visual cortex (V1b) (Hengen et al., 2013; Kaneko et al., 2008; Keck et al., 2013; Mrsic-Flogel et al., 2007). The possibility that defects in this robust homeostatic compensation might render central circuits vulnerable to perturbations has not been carefully examined in any ASD model.

Our data demonstrate that loss of the major neocortical isoforms of Shank3 results in simultaneous loss of synaptic and intrinsic homeostatic plasticity in neocortical pyramidal neurons. Surprisingly, these deficits can be rescued *in vitro* by treatment with lithium (Li) or by pharmacological inhibition of the Li target glycogen synthase kinase 3 (GSK3). Multielectrode array recordings in freely behaving Shank3 knockout mice demonstrate that these homeostatic defects result in dramatic loss of FRH. In addition, the late

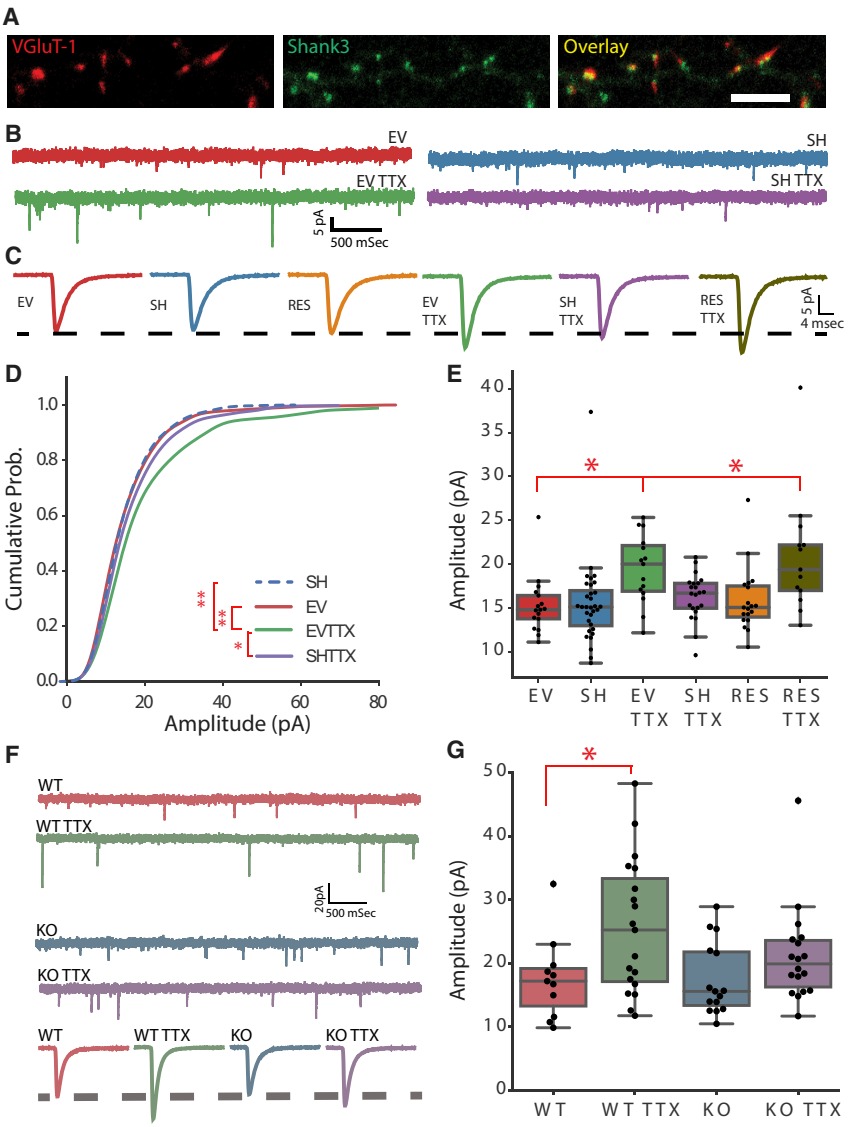

Figure 1. Block of Synaptic Scaling by Shank3 Loss

(A) Representative images of dendrites immunolabled for VGluT1 (red) and Shank3 (green). Scale bar, 5 μm.

(B and C) Synaptic scaling in Shank3 KD neurons: example raw mEPSC traces (B) and average mEPSC waveforms (C) for the indicated conditions.

(D and E) Cumulative histograms of mEPSC amplitudes (D) and mean mEPSC amplitude (E) for the indicated conditions (n: EV = 17, EV TTX = 15, SH = 32, SH TTX = 22, RES = 19, RES TTX = 13).

(F and G) Synaptic scaling in *Shank3b*$^{-/-}$ neurons: example raw traces and average mEPSC waveforms (F) and mean mEPSC amplitude (G) (n: WT = 11, WT TTX = 20, KO = 15, KO TTX = 18).

See also Figures S1 and S2. Here and below, boxplots depict first and third quartiles of the data, and whiskers show the remainder of the distribution. Line depicts median; points represent all data points. *p < 0.05, **p < 0.01, ****p < 0.00; p > 0.5 is considered not significant (N.S.). Statistical tests and actual p values for each comparison here and below are given in Table S1.

(homeostatic) phase of OD plasticity, which normally restores the net drive from the two eyes (Espinosa and Stryker, 2012; Mrsic-Flogel et al., 2007), was disrupted in Shank3 knockout mice. Finally, treatment of Shank3 knockout mice with Li ameliorated a robust overgrooming phenotype (Bey et al., 2018; Peça et al., 2011; Zhou et al., 2016), suggesting that restoring homeostatic plasticity has some behavioral benefit. These results support a causal relationship between loss of homeostatic mechanisms and deficits in homeostatic compensation to sensory perturbations. Furthermore, they suggest that loss of cellular mechanisms of homeostatic plasticity may contribute to the development of circuit and, ultimately, behavioral disfunctions in ASDs.

RESULTS

Shank3 Is Required for Synaptic Scaling

Shank3 is enriched at postsynaptic sites (Figure 1A), where it interacts with a number of synaptic scaling effector proteins (Monteiro and Feng, 2017). To determine whether a normal complement of Shank3 is necessary for synaptic scaling, we used RNAi to induce acute and sparse knockdown (KD) in rat visual cortical cultures using a short hairpin (SH) that targets most isoforms of Shank3 (Verpelli et al., 2011). This approach reduced Shank3 levels to ~50% of control levels in a small number of individual pyramidal neurons, whereas the vast majority of neurons were unaffected, allowing us to probe the cell-autonomous effect of Shank3 loss (Figures S1A and S1B). Synaptic scaling is characterized by multiplicative shifts in the amplitude distribution of α-amino-3-hydroxy-5-methyl-4-isoxazolepropionic acid receptor (AMPAR)-mediated miniature excitatory postsynaptic currents (mEPSCs; Turrigiano et al., 1998; Figure 1). which are a measure of the postsynaptic strength of excitatory synapses. Whole-cell recordings of mEPSCs in Shank3 KD neurons (SH) revealed no significant effect of Shank3 KD on the basal mEPSC amplitude compared with empty vector (EV) controls (Figures 1B–1E) or on mEPSC frequency or excitatory synapse density (Figures S1F and S1G); mEPSCs recorded from L2/3 pyramidal neurons in acute V1 slices were also similar between wild-type (WT) and *Shank3b*$^{-/-}$ knockout (KO) mice (Figure S4C; Peça et al., 2011).

In contrast to the lack of effect on basal mEPSC properties, synaptic scaling up was completely abolished by Shank3 KD. Blocking spikes with tetrodotoxin (TTX) for 24 h scaled up mEPSC amplitude in EV neurons but not in Shank3 KD neurons (Figures 1B–1E). Shank3 KD also prevented the changes in AMPAR synaptic accumulation known to drive neocortical synaptic scaling (Figures S1C–S1E; Gainey et al., 2009, 2015;

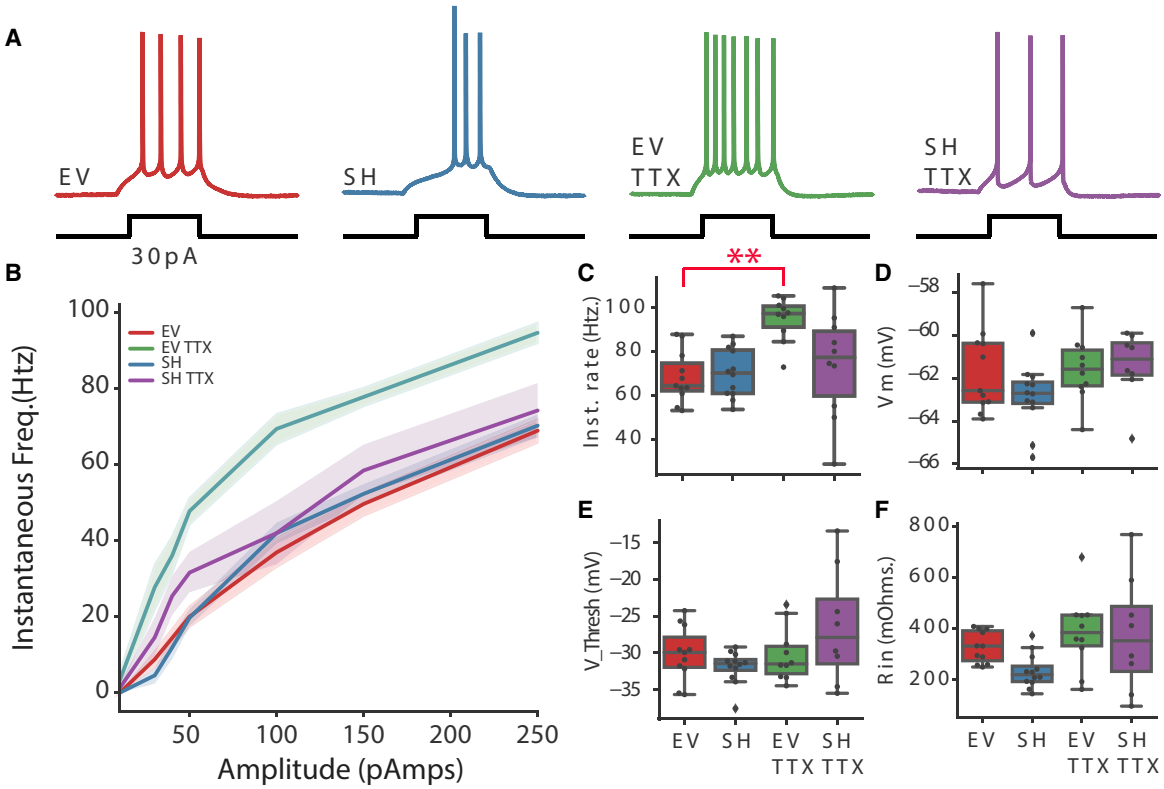

Figure 2. Shank3 Loss Prevents Intrinsic Homeostatic Plasticity

(A) Example firing for neurons under the indicated conditions.

(B) Average *f-I* curves for the indicated conditions. Shaded areas around curves denote standard error.

(C) Average instantaneous firing rates for the indicated conditions during the highest current injection (250 pA) (n: EV = 11, EV TTX = 10, SH = 12, SH TTX = 8).

(D–F) Passive neuronal properties across conditions, showing Vm (D), VThresh (voltage threshold for action potential firing) (E), and Rin (F).

See also Figures S2 and S4.

Ibata et al., 2008). Synaptic scaling could be rescued by co-expression of an RNAi-resistant form of Shank3 (Figure 1E, resistant [RES]), ruling out off-target effects of the short hairpin RNA (shRNA). Thus, a 50% loss of Shank3 (analogous to haploinsufficiency in human shankopathies) is sufficient to completely abolish synaptic scaling, and this requirement is cell autonomous. As a second means of testing the necessity of Shank3 in synaptic scaling, we made cultures from visual cortices of *Shank3b*$^{-/-}$ (Figures 4F and 4G), *Shank3b*$^{+/-}$, or WT littermate mice (Figure S4E). Although neurons from *Shank3b*$^{-/-}$ and *Shank3b*$^{+/-}$ mice had similar basal mEPSC amplitudes as WT littermate neurons (as reported previously; Chiesa et al., 2019; Peça et al., 2011), in KO neurons, TTX induced only a small and non-significant increase in mEPSC amplitude (Figures 1F and 1G; Figure S4E).

Shank3 Is Required for Homeostatic Regulation of Intrinsic Excitability

Shank3 interacts with ion channels as well as synaptic scaffold proteins (Yi et al., 2016), but the possibility that intrinsic homeostatic plasticity is impaired in shankopathies has not been explored. To determine whether Shank3 is essential for intrinsic homeostatic plasticity, we knocked down Shank3 sparsely in individual cultured neurons as before (Figures S1A and S1B), blocked spiking with TTX for 24 h, and then probed intrinsic excitability by generating firing rate vs current (*f-I*) curves in the presence of synaptic blockers (Figure 2). After TTX treatment, the same current injection evoked more action potentials in EV neurons (Figure 2A), and the entire FI curve shifted significantly upward and leftward (Figure 2B), as expected (Desai et al., 1999). In contrast, TTX had no effect on excitability in Shank3 KD neurons (Figures 2B and 2C), indicating that intrinsic homeostatic plasticity is absent. Interestingly, although in hippocampal pyramidal neurons Shank3 KO reduces a hyperpolarization-activated cation current (I_h) and, thus, increases input resistance (Yi et al., 2016), in these V1 pyramidal neurons Shank3 KD had no significant effect on passive neuronal properties (Figures 2D–2F) or on basal intrinsic excitability (Figures 2B and 2C); similarly, input resistance was not altered in L2/3 pyramidal neurons from Shank3 KO mice relative to WT littermates (Figure S2F).

Synaptic and Intrinsic Homeostatic Plasticity Defects Caused by Shank3 KD Can Be Restored by Li Treatment

Li has wide efficacy to treat many neurological disorders, but the mechanism of action is debated (Pisanu et al., 2016). Recent

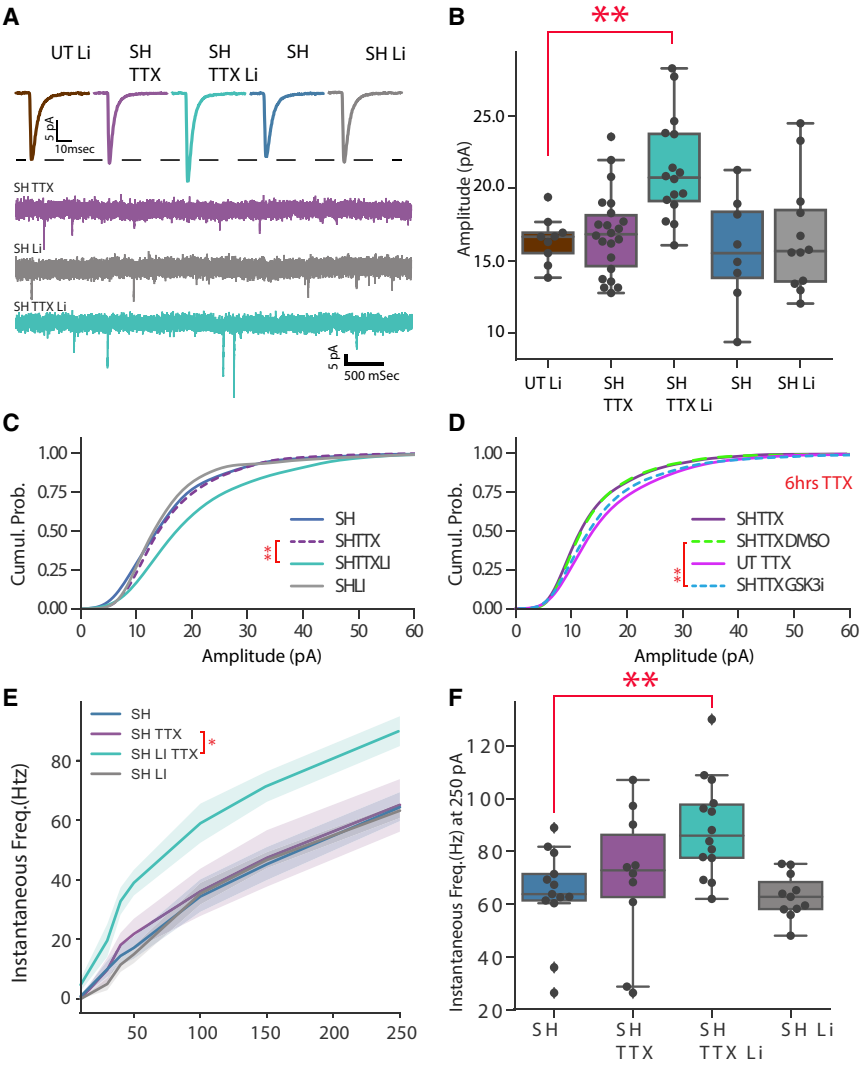

Figure 3. Li Treatment Rescues Intrinsic and Synaptic Homeostatic Plasticity

(A) Average mEPSC traces (top) and example raw traces (bottom) from control or KD neurons treated with Li or Li and TTX for 24 h.

(B) Mean mEPSC amplitudes (n: Li = 9, SH TTX = 22, SH TTX Li = 16, SH = 8, SH Li = 12).

(C) Cumulative histograms of mEPSCs for the conditions in (B).

(D) Cumulative histograms from neurons treated for 6 h with TTX and DMSO (vehicle) or TTX and 5 μM GSK3 inhibitor (GSK3i) (n: UT [untransfected] TTX = 30, SH TTX = 25, SH TTX DMSO = 31, SH TTX GSK3i = 30. SH TTX GSK3i versus SH TTX DMSO (**).

(E) Li rescue: *f-I* curves for the indicated conditions.

(F) Average firing rates from the conditions in (E) at the highest current injection (250 pA) (n: SH = 13, SH TTX = 10, SH TTX Li = 14, SH Li = 11).

See also Figure S3.

case studies have raised the possibility that Li might alleviate some neuropsychiatric symptoms in human shankopathies (Darville et al., 2016; Egger et al., 2017; Serret et al., 2015), leading us to wonder whether Li might rescue the defects in homeostatic plasticity induced by Shank3 loss. After 24-h incubation with a therapeutic dose (1 mM) of LiCl, Shank3 KD neurons were again able to fully express synaptic scaling (Figures 3A–3C). Li did not exert these effects through simple global enhancement of synaptic scaling because Li treatment had no effect on the magnitude of scaling in control neurons with a normal Shank3 complement (Figures S3A–S3D). Further, Li had no significant effect on basal postsynaptic (Figures S3B and S3C) or neuronal (Figures S2A and S2B) properties. Strikingly, Li treatment was also able to rescue intrinsic homeostatic plasticity (Figures 3E and 3F); the TTX-induced shift in the FI curve for Shank3 KD neurons treated with Li was similar to that of control neurons (curves not significantly different; Figure S3G).

In addition to rescuing synaptic scaling after Shank3 KD, Li treatment was also able to rescue synaptic scaling in KO mouse cultures (Figure S3F), suggesting that Li is functioning downstream of Shank3 in the signaling pathways that regulate synaptic scaling. Li acts as a direct and indirect inhibitor of GSK3 through inhibitory phosphorylation of Ser9/21 (Freland and Beaulieu, 2012); we therefore tested whether a highly specific GSK3 inhibitor (GSK3i), BRD0320, which blocks GSK3 alpha and beta but not other closely related kinases (Wagner et al., 2016), could rescue synaptic scaling. Like Li, BRD0320 was able to rescue synaptic scaling in Shank3 KD neurons (Figure 3D), suggesting that the GSK3 pathway is dysregulated by Shank3 loss in neocortical pyramidal neurons and that this dysregulation contributes to the observed defect in synaptic scaling.

Shank3 KO Mice Have Deficits in FRH and OD Plasticity

A well-described function of synaptic scaling and intrinsic homeostatic plasticity *in vivo* is to slowly restore firing rates (FRH) and rebalance sensory drive following sensory perturbations (Hengen et al., 2013; Kaneko et al., 2008; Keck et al., 2013; Mrsic-Flogel et al., 2007; Turrigiano, 2017). Given that loss of Shank3 disrupts both of these major forms of homeostatic plasticity, we wondered whether compensatory plasticity during MD *in vivo* would also be disrupted. Initially we examined FRH by implanting critical-period Shank3 KO or littermate WT mice with multielectrode arrays in the V1m, performed MD as described (Hengen et al., 2013, 2016), and followed changes in firing rates over time in freely behaving animals. In both WT and KO animals, the distributions of baseline firing rates were wide, as expected (Darville et al., 2016; Peixoto et al., 2016), and were only subtly different between WT and KO littermates (Figure 4A).

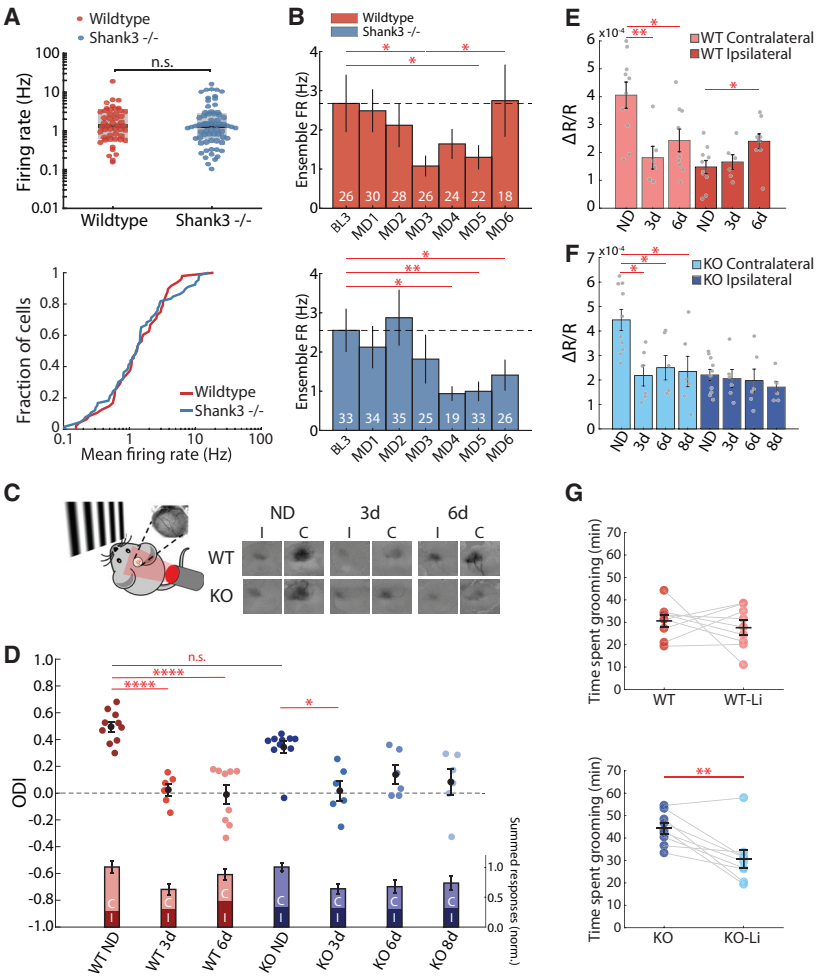

Figure 4. Shank3 Is Required for FRH and OD Plasticity *In Vivo*

(A) Baseline mean ensemble firing rates (top) and cumulative distribution of firing rates (bottom) for V1 neurons in freely behaving Shank3b WT mice and KO littermates.

(B) Ensemble firing rate (hertz) across baseline and 6-day MD. Bars show mean ± SEM; numbers indicate the number of cells recorded on that day.

(C) Schematic of intrinsic signal optical imaging (left) and representative changes in reflectance in response to drive through either the ipsilateral (I) or contralateral (C) eye for both genotypes after no (ND), 3 days, or 6 days of MD.

(D) ODI values for each genotype (WT and KO) for ND, 3-day, or 6-day MD. Inset: summed responses from both eyes, normalized to ND conditions by genotype.

(E and F) Responses to C or I visual drive in WT (E) or KO (F) animals.

(G) Cumulative time spent grooming during a 3 h period, before and after 1 week Li treatment for WT mice (top, n = 9) and Shank3 KO littermates (bottom, n = 9). Grey lines connect data from same mouse; black lines and error bars indicate mean ± SEM.

See also Figure S4.

In freely behaving WT mice, MD resulted in biphasic changes in firing of V1m neurons, as expected (Hengen et al., 2013, 2016): first a drop in mean firing rates that reached a minimum after 3 days of MD (because of suppressive Hebbian mechanisms induced by blurred vision through the closed eye; Smith et al., 2009), followed by homeostatic restoration of firing rates back to baseline values (Figure 4B). This drop was a little slower than described previously in the rat V1m, where the minimum firing rate is on MD 2 (Hengen et al., 2013, 2016). The behavior of neurons in Shank3B KO mice was strikingly different from WT neurons: mean firing rates dropped as for WT animals (although more slowly, reaching a nadir after 4 days of MD), and there was no recovery in firing rates over the ensuing 2 days (Figure 4B). In WT animals, the entire distribution of firing rates initially shifted to the left and then recovered, so that, by MD6, the distribution was statistically indistinguishable from baseline (Figure S4B). In contrast, in Shank3 KO mice, the distribution shifted to the left, and there was little recovery by MD6 (Figure S4A).

In the V1b, MD induces shifts in visual drive from the two eyes that is also biphasic; 3-day MD induces a Hebbian depression of closed (contralateral [C]) eye responses, followed by a homeostatic increase in responsiveness to the open (ipsilateral [I]) eye (Espinosa and Stryker, 2012; Frenkel and Bear, 2004; Gordon and Stryker, 1996; Kaneko et al., 2008; Smith et al., 2009) so that total drive from the two eyes after 6-day MD is restored close to the non-deprived (ND) condition (Figure 4D, WT inset, Mrsic-Flogel et al., 2007). Together, these changes result in shifts in the OD index (ODI; defined as (C−I)/(C+I); Figures 4C and 4D). As a second means of measuring homeostatic recovery in Shank3 KO mice, we therefore performed MD on KO and WT littermates and measured OD shifts in the V1b using intrinsic signal imaging (Figures 4C and 4D; Cang et al., 2005; Moore et al., 2018). In both WT and KO mice, MD shifted ODI toward the open eye (Figure 4D), but the contribution of the two eyes to this shift was distinct in the two genotypes (Figures 4D, inset, 4E, and 4F). Both WT and KO mice exhibited the normal loss of responsiveness to the C eye after 3-day MD, but although WT mice showed the expected increase in I eye responses after 6-day MD (Figure 4E), Shank3 KO mice failed to show this homeostatic increase (Figure 4F). An important question is whether homeostatic compensation is missing in Shank3 KO mice or whether the compensation is simply slower. To address this, we performed MD for 8 days in KO mice and again measured responsiveness to visual stimulation of the two eyes; even after longer deprivation, there was no homeostatic increase in I responsiveness (Figure 4F). Thus, loss of Shank3 severely compromises the ability of neocortical neurons to undergo homeostatic recovery after perturbations to sensory drive.

Overgrooming in Shank3 KO Mice Is Corrected by Li Treatment

We hypothesized that loss of homeostatic plasticity in Shank3 KO mice might contribute to behavioral phenotypes of these mice; if so, then Li treatment should restore WT behavior in KO mice. One robust behavioral phenotype of the Shank3b KO mouse is excessive grooming that can lead to self-injury (Peça et al., 2011); this phenotype has also been observed in several other Shank3 KO and/or loss-of-function mice (Bey et al., 2018; Peça et al., 2011; Zhou et al., 2016). Consistent with previously published results, baseline grooming was higher in KO mice than in WT littermates (Figures 4G; Figure S4D). Next we put WT and KO animals on a Li chow diet for 1 week as described (O'Brien and Klein, 2009) and then measured grooming behavior again in the same pairs. Li did not affect grooming in WT mice but reduced grooming in KO mice close to WT levels (Figure 4G). Thus, Li, which rescues homeostatic plasticity in Shank3 KO and KD neurons, is also able to correct overgrooming in Shank3 KO mice.

DISCUSSION

Homeostatic compensation is widely considered essential for neurons and circuits to maintain stable function in response to experience-dependent perturbations in drive (Abbott and Nelson, 2000; Davis, 2013; Marder and Goaillard, 2006; Turrigiano and Nelson, 2004). Here we show that loss of Shank3 abolishes cellular forms of homeostatic plasticity in neocortical pyramidal neurons and homeostatic compensation to sensory perturbations in visual cortical circuits. These data suggest that a major sequela of Shank3 loss is the inability of central circuits to harness homeostatic plasticity to compensate for perturbations in drive.

Shank3 haploinsufficiency is strongly associated with ASDs and intellectual disability (Betancur and Buxbaum, 2013), and Shank3 loss in mice generates a range of behavior phenotypes, from excessive self-grooming to abnormalities in social behavior (Bey et al., 2018; Bozdagi et al., 2010; Duffney et al., 2015; Jaramillo et al., 2017; Kouser et al., 2013; Lee et al., 2015; Orefice et al., 2016; Peça et al., 2011; Schmeisser et al., 2012; Wang et al., 2011; Yang et al., 2012); the exact phenotypes observed likely depend on the KO strategy used because different mouse models show different patterns of loss of alternatively spliced isoforms (Jiang and Ehlers, 2013; Monteiro and Feng, 2017; Speed et al., 2015; Wang et al., 2016; Zhou et al., 2016). The RNAi and KO mouse models we use here strongly reduce the major neocortical isoforms of Shank3 (Peça et al., 2011; Verpelli et al., 2011), and we find that an ~50% loss is sufficient to completely abolish homeostatic plasticity *in vitro*. Overexpression of Shank3 can induce phenotypes (Han et al., 2013; Harris et al., 2016), but cell-autonomous overexpression had no effect on synaptic scaling, suggesting that too little and too much Shank3 disrupt circuit function through distinct mechanisms.

Acute, cell-autonomous loss of Shank3 is sufficient to completely block synaptic scaling and intrinsic homeostatic plasticity but has little effect on basal synaptic or intrinsic properties in neocortical pyramidal neurons. This suggests that acute Shank3 loss disrupts a signaling pathway or pathways critical for expression of homeostatic adjustments rather than directly perturbing excitability. We also observed little effect of global Shank3 KO on basal excitability, synaptic properties, or visual function in the V1 at the ages studied here (the classical visual system critical period, post-natal day 25 [P25]–P32). Our observation that basal visual drive from the two eyes is relatively normal in Shank3 KO mice is consistent with a recent study demonstrating that several other monogenic ASD mouse models (FMR1, Cntnap2, 16p11.2del, and Tsc2) have only subtle baseline defects in whisker drive to the somatosensory cortex (Antoine et al., 2019); because this study did not perturb sensory experience, it is unknown whether these mice have defects in homeostatic compensation following sensory perturbations.

The complete signaling pathway through which Shank3 loss disrupts homeostatic plasticity remains to be elucidated, but the ability of Li—and inhibition of Li's known target GSK3—to rescue homeostatic plasticity strongly implicates dysregulation of GSK3 in this process and is consistent with a recent study showing reduced inhibitory phosphorylation of GSK3 following Shank3 KD (Bidinosti et al., 2016). Li is still the first-line treatment for bipolar disorder and can be efficacious in the treatment of other neuropsychiatric disorders that are unresponsive to standard medications (Rybakowski, 2011), including some case studies of human shankopathies (Egger et al., 2017; Serret et al., 2015). However, despite decades of therapeutic use, there is still little understanding of Li's mode of action. Li treatment has complex effects on AMPA receptor function that depend on cell type and treatment length. For example, chronic Li treatment decreases synaptic AMPAR levels and reduces AMPA-mediated quantal amplitude (Ankolekar and Sikdar, 2015; Du et al., 2003; Gideons et al., 2017; Gray et al., 2003), whereas shorter treatments (16–20 h of 2 mM) increase (Farooq et al., 2017) or decrease (Gray et al., 2003) surface GluA2 levels. Some differences between studies may reflect distinct responses of different neuronal types, because feeding mice Li chow increases AMPAR accumulation in hippocampal but not neocortical neurons (Gould et al., 2008). We find that Li treatment (24 h at 1 mM) affects neither the basal mEPSC amplitude nor the intrinsic excitability of neocortical pyramidal neurons but completely rescues the expression of homeostatic plasticity. Although it seems likely that chronic Li treatment has additional targets beyond restoration of homeostatic plasticity, taken together, our data raise the possibility that rescue of homeostatic plasticity is one important mechanism of action of Li therapy.

Synaptic scaling and intrinsic homeostatic plasticity are known to play essential stabilizing functions during experience-dependent plasticity in sensory systems (Gainey and Feldman, 2017), and although their roles in other brain regions remain largely unexplored, they are widely expressed (Glazewski et al., 2017; Keck et al., 2017). An important question is how Shank3-mediated loss of homeostatic plasticity contributes to the genesis of microcircuit defects in circuits outside of the sensory cortex, where Shank3 KO is known to affect synaptic properties and excitability in a number of brain regions (Jiang and Ehlers, 2013; Kouser et al., 2013; Peixoto et al., 2016;

Wang et al., 2017; Zhu et al., 2018). Many brain regions, including the striatum, cerebellum, neocortex, and amygdala, are involved in the patterning and modulation of self-grooming behavior (Kalueff et al., 2016). The ability of Li to restore the duration of self-grooming to WT levels in Shank3 KO mice raises the possibility that homeostatic mechanisms play a role in regulating interactions within and between these circuits to maintain normal levels of self-grooming.

STAR★METHODS

Detailed methods are provided in the online version of this paper and include the following:

- KEY RESOURCES TABLE
- LEAD CONTACT AND MATERIALS AVAILABILITY
- EXPERIMENTAL MODEL AND SUBJECT DETAILS
- METHOD DETAILS
  - Primary cortical neuron culture
  - Immunocytochemistry and Image analysis
  - Culture Electrophysiology
  - Slice Electrophysiology
  - Reagents
  - DNA constructs
  - Surgery and *in vivo* recordings
  - Histology
  - *In vivo* data analysis
  - Intrinsic Signal Imaging
  - Grooming behavior assay
- QUANTIFICATION AND STATISTICAL ANALYSIS
- DATA AND CODE AVAILABLITY

SUPPLEMENTAL INFORMATION

Supplemental Information can be found online at https://doi.org/10.1016/j.neuron.2020.02.033.

ACKNOWLEDGMENTS

We thank Dr. Chiara Verpelli for Shank3 constructs; Lirong Wang, Genelle Rankin, Jorden Rabasco, and Hannah BenDavid for technical support; and Ted Brookings for the MATLAB program for analyzing *f-I* data. This work was supported by Simons Foundation award 345485 (to G.G.T.) and National Institutes of Health awards R35 NS111562 (to G.G.T.), R01 EY025613 (to G.G.T.), and R01 EY022122 (to S.D.V.H.).

AUTHOR CONTRIBUTIONS

Conceptualization, V.T. and G.G.T.; Methodology and Software, V.T., G.G.T., A.T.P., K.B.H., and S.D.V.H.; Investigation, V.T., A.T.P., C.G.K., K.B.H., N.J.M., and H.L.; Formal Analysis, V.T., A.T.P., C.G.K., N.J.M., and H.L.; Writing, V.T., G.G.T., and A.T.P.; Visualization, V.T. and A.T.P.; Resources, F.F.W.; Supervision, Administration, and Funding, G.G.T. and S.D.V.H.

DECLARATION OF INTERESTS

The authors declare no competing interests.

Received: August 28, 2018
Revised: February 4, 2020
Accepted: February 26, 2020
Published: March 20, 2020

REFERENCES

Abbott, L.F., and Nelson, S.B. (2000). Synaptic plasticity: taming the beast. Nat. Neurosci. *3* (*Suppl*), 1178–1183.

Ankolekar, S.M., and Sikdar, S.K. (2015). Early postnatal exposure to lithium in vitro induces changes in AMPAR mEPSCs and vesicular recycling at hippocampal glutamatergic synapses. J. Biosci. *40*, 339–354.

Antoine, M.W., Langberg, T., Schnepel, P., and Feldman, D.E. (2019). Increased Excitation-Inhibition Ratio Stabilizes Synapse and Circuit Excitability in Four Autism Mouse Models. Neuron *101*, 648–661.

Bariselli, S., Tzanoulinou, S., Glangetas, C., Prévost-Solié, C., Pucci, L., Viguié, J., Bezzi, P., O'Connor, E.C., Georges, F., Lüscher, C., and Bellone, C. (2016). SHANK3 controls maturation of social reward circuits in the VTA. Nat. Neurosci. *19*, 926–934.

Betancur, C., and Buxbaum, J.D. (2013). SHANK3 haploinsufficiency: a "common" but underdiagnosed highly penetrant monogenic cause of autism spectrum disorders. Mol. Autism *4*, 17.

Bey, A.L., Wang, X., Yan, H., Kim, N., Passman, R.L., Yang, Y., Cao, X., Towers, A.J., Hulbert, S.W., Duffney, L.J., et al. (2018). Brain region-specific disruption of Shank3 in mice reveals a dissociation for cortical and striatal circuits in autism-related behaviors. Transl. Psychiatry *8*, 94.

Bidinosti, M., Botta, P., Krüttner, S., Proenca, C.C., Stoehr, N., Bernhard, M., Fruh, I., Mueller, M., Bonenfant, D., Voshol, H., et al. (2016). CLK2 inhibition ameliorates autistic features associated with SHANK3 deficiency. Science *351*, 1199–1203.

Blackman, M.P., Djukic, B., Nelson, S.B., and Turrigiano, G.G. (2012). A critical and cell-autonomous role for MeCP2 in synaptic scaling up. J. Neurosci. *32*, 13529–13536.

Bozdagi, O., Sakurai, T., Papapetrou, D., Wang, X., Dickstein, D.L., Takahashi, N., Kajiwara, Y., Yang, M., Katz, A.M., Scattoni, M.L., et al. (2010). Haploinsufficiency of the autism-associated Shank3 gene leads to deficits in synaptic function, social interaction, and social communication. Mol. Autism *1*, 15.

Bulow, P., Murphy, T.J., Bassell, G.J., and Wenner, P. (2019). Homeostatic Intrinsic Plasticity Is Functionally Altered in Fmr1 KO Cortical Neurons. Cell Rep. *26*, 1378–1388.e3.

Cang, J., Kalatsky, V.A., Löwel, S., and Stryker, M.P. (2005). Optical imaging of the intrinsic signal as a measure of cortical plasticity in the mouse. Vis. Neurosci. *22*, 685–691.

Chiesa, M., Nardou, R., Lozovaya, N., Eftekhari, S., Tyzio, R., Guimond, D., Ferrari, D.C., and Ben-Ari, Y. (2019). Enhanced Glutamatergic Currents at Birth in Shank3 KO Mice. Neural Plast. *2019*, 2382639.

Dani, V.S., Chang, Q., Maffei, A., Turrigiano, G.G., Jaenisch, R., and Nelson, S.B. (2005). Reduced cortical activity due to a shift in the balance between excitation and inhibition in a mouse model of Rett syndrome. Proc. Natl. Acad. Sci. USA *102*, 12560–12565.

Darville, H., Poulet, A., Rodet-Amsellem, F., Chatrousse, L., Pernelle, J., Boissart, C., Héron, D., Nava, C., Perrier, A., Jarrige, M., et al. (2016). Human Pluripotent Stem Cell-derived Cortical Neurons for High Throughput Medication Screening in Autism: A Proof of Concept Study in SHANK3 Haploinsufficiency Syndrome. EBioMedicine *9*, 293–305.

Davis, G.W. (2013). Homeostatic signaling and the stabilization of neural function. Neuron *80*, 718–728.

Desai, N.S., Rutherford, L.C., and Turrigiano, G.G. (1999). Plasticity in the intrinsic excitability of cortical pyramidal neurons. Nat. Neurosci. *2*, 515–520.

Du, J., Gray, N.A., Falke, C., Yuan, P., Szabo, S., and Manji, H.K. (2003). Structurally dissimilar antimanic agents modulate synaptic plasticity by regulating AMPA glutamate receptor subunit GluR1 synaptic expression. Ann. N Y Acad. Sci. *1003*, 378–380.

Duffney, L.J., Zhong, P., Wei, J., Matas, E., Cheng, J., Qin, L., Ma, K., Dietz, D.M., Kajiwara, Y., Buxbaum, J.D., and Yan, Z. (2015). Autism-like Deficits in Shank3-Deficient Mice Are Rescued by Targeting Actin Regulators. Cell Rep. *11*, 1400–1413.

Egger, J.I.M., Verhoeven, W.M.A., Groenendijk-Reijenga, R., and Kant, S.G. (2017). Phelan-McDermid syndrome due to *SHANK3* mutation in an intellectually disabled adult male: successful treatment with lithium. BMJ Case Rep. *2017*.

Espinosa, J.S., and Stryker, M.P. (2012). Development and plasticity of the primary visual cortex. Neuron *75*, 230–249.

Farooq, M., Kim, S., Patel, S., Khatri, L., Hikima, T., Rice, M.E., and Ziff, E.B. (2017). Lithium increases synaptic GluA2 in hippocampal neurons by elevating the δ-catenin protein. Neuropharmacology *113* (Pt A), 426–433.

Freland, L., and Beaulieu, J.M. (2012). Inhibition of GSK3 by lithium, from single molecules to signaling networks. Front. Mol. Neurosci. *5*, 14.

Frenkel, M.Y., and Bear, M.F. (2004). How monocular deprivation shifts ocular dominance in visual cortex of young mice. Neuron *44*, 917–923.

Friard, O., and Gamba, M. (2016). BORIS: a free, versatile open-source event-logging software for video/audio coding and live observations. Methods in Ecology and Evolution. https://doi.org/10.1111/2041-210X.12584.

Gainey, M.A., and Feldman, D.E. (2017). Multiple shared mechanisms for homeostatic plasticity in rodent somatosensory and visual cortex. Philos. Trans. R. Soc. Lond. B Biol. Sci. *372*.

Gainey, M.A., Hurvitz-Wolff, J.R., Lambo, M.E., and Turrigiano, G.G. (2009). Synaptic scaling requires the GluR2 subunit of the AMPA receptor. J. Neurosci. *29*, 6479–6489.

Gainey, M.A., Tatavarty, V., Nahmani, M., Lin, H., and Turrigiano, G.G. (2015). Activity-dependent synaptic GRIP1 accumulation drives synaptic scaling up in response to action potential blockade. Proc. Natl. Acad. Sci. USA *112*, E3590–E3599.

Gamba, O.F.M. (2016). BORIS: a free, versatile open-source event-logging software for video/audio coding and live observations. Methods Ecol. Evol. *7*, 1325–1330.

Geramita, M., and Urban, N.N. (2016). Postnatal Odor Exposure Increases the Strength of Interglomerular Lateral Inhibition onto Olfactory Bulb Tufted Cells. J. Neurosci. *36*, 12321–12327.

Gideons, E.S., Lin, P.Y., Mahgoub, M., Kavalali, E.T., and Monteggia, L.M. (2017). Chronic lithium treatment elicits its antimanic effects via BDNF-TrkB dependent synaptic downscaling. eLife *6*.

Glazewski, S., Greenhill, S., and Fox, K. (2017). Time-course and mechanisms of homeostatic plasticity in layers 2/3 and 5 of the barrel cortex. Philos. Trans. R. Soc. Lond. B Biol. Sci. *372*.

Gordon, J.A., and Stryker, M.P. (1996). Experience-dependent plasticity of binocular responses in the primary visual cortex of the mouse. J. Neurosci. *16*, 3274–3286.

Gould, T.D., O'Donnell, K.C., Dow, E.R., Du, J., Chen, G., and Manji, H.K. (2008). Involvement of AMPA receptors in the antidepressant-like effects of lithium in the mouse tail suspension test and forced swim test. Neuropharmacology *54*, 577–587.

Gray, N.A., Zhou, R., Du, J., Moore, G.J., and Manji, H.K. (2003). The use of mood stabilizers as plasticity enhancers in the treatment of neuropsychiatric disorders. J. Clin. Psychiatry *64* (*Suppl 5*), 3–17.

Han, K., Holder, J.L., Jr., Schaaf, C.P., Lu, H., Chen, H., Kang, H., Tang, J., Wu, Z., Hao, S., Cheung, S.W., et al. (2013). SHANK3 overexpression causes manic-like behaviour with unique pharmacogenetic properties. Nature *503*, 72–77.

Harris, K.D., Henze, D.A., Csicsvari, J., Hirase, H., and Buzsáki, G. (2000). Accuracy of tetrode spike separation as determined by simultaneous intracellular and extracellular measurements. J. Neurophysiol. *84*, 401–414.

Harris, K.P., Akbergenova, Y., Cho, R.W., Baas-Thomas, M.S., and Littleton, J.T. (2016). Shank Modulates Postsynaptic Wnt Signaling to Regulate Synaptic Development. J. Neurosci. *36*, 5820–5832.

Hengen, K.B., Lambo, M.E., Van Hooser, S.D., Katz, D.B., and Turrigiano, G.G. (2013). Firing rate homeostasis in visual cortex of freely behaving rodents. Neuron *80*, 335–342.

Hengen, K.B., Torrado Pacheco, A., McGregor, J.N., Van Hooser, S.D., and Turrigiano, G.G. (2016). Neuronal Firing Rate Homeostasis Is Inhibited by Sleep and Promoted by Wake. Cell *165*, 180–191.

Ibata, K., Sun, Q., and Turrigiano, G.G. (2008). Rapid synaptic scaling induced by changes in postsynaptic firing. Neuron *57*, 819–826.

Jaramillo, T.C., Speed, H.E., Xuan, Z., Reimers, J.M., Escamilla, C.O., Weaver, T.P., Liu, S., Filonova, I., and Powell, C.M. (2017). Novel Shank3 mutant exhibits behaviors with face validity for autism and altered striatal and hippocampal function. Autism Res. *10*, 42–65.

Jiang, Y.H., and Ehlers, M.D. (2013). Modeling autism by SHANK gene mutations in mice. Neuron *78*, 8–27.

Joseph, A., and Turrigiano, G.G. (2017). All for One But Not One for All: Excitatory Synaptic Scaling and Intrinsic Excitability Are Coregulated by CaMKIV, Whereas Inhibitory Synaptic Scaling Is Under Independent Control. J. Neurosci. *37*, 6778–6785.

Kalueff, A.V., Aldridge, J.W., LaPorte, J.L., Murphy, D.L., and Tuohimaa, P. (2007). Analyzing grooming microstructure in neurobehavioral experiments. Nat. Protoc. *2*, 2538–2544.

Kalueff, A.V., Stewart, A.M., Song, C., Berridge, K.C., Graybiel, A.M., and Fentress, J.C. (2016). Neurobiology of rodent self-grooming and its value for translational neuroscience. Nat. Rev. Neurosci. *17*, 45–59.

Kaneko, M., Stellwagen, D., Malenka, R.C., and Stryker, M.P. (2008). Tumor necrosis factor-alpha mediates one component of competitive, experience-dependent plasticity in developing visual cortex. Neuron *58*, 673–680.

Keck, T., Keller, G.B., Jacobsen, R.I., Eysel, U.T., Bonhoeffer, T., and Hübener, M. (2013). Synaptic scaling and homeostatic plasticity in the mouse visual cortex in vivo. Neuron *80*, 327–334.

Keck, T., Toyoizumi, T., Chen, L., Doiron, B., Feldman, D.E., Fox, K., Gerstner, W., Haydon, P.G., Hübener, M., Lee, H.K., et al. (2017). Integrating Hebbian and homeostatic plasticity: the current state of the field and future research directions. Philos. Trans. R. Soc. Lond. B Biol. Sci. *372*.

Kouser, M., Speed, H.E., Dewey, C.M., Reimers, J.M., Widman, A.J., Gupta, N., Liu, S., Jaramillo, T.C., Bangash, M., Xiao, B., et al. (2013). Loss of predominant Shank3 isoforms results in hippocampus-dependent impairments in behavior and synaptic transmission. J. Neurosci. *33*, 18448–18468.

Lambo, M.E., and Turrigiano, G.G. (2013). Synaptic and Intrinsic Homeostatic Mechanisms Cooperate to Increase L2/3 Pyramidal Neuron Excitability During a Late Phase of Critical Period Plasticity. J Neurosci *33*, 8810–8819.

Lee, J., Chung, C., Ha, S., Lee, D., Kim, D.Y., Kim, H., and Kim, E. (2015). Shank3-mutant mice lacking exon 9 show altered excitation/inhibition balance, enhanced rearing, and spatial memory deficit. Front. Cell. Neurosci. *9*, 94.

Marder, E., and Goaillard, J.M. (2006). Variability, compensation and homeostasis in neuron and network function. Nat. Rev. Neurosci. *7*, 563–574.

Monteiro, P., and Feng, G. (2017). SHANK proteins: roles at the synapse and in autism spectrum disorder. Nat. Rev. Neurosci. *18*, 147–157.

Moore, A.R., Richards, S.E., Kenny, K., Royer, L., Chan, U., Flavahan, K., Van Hooser, S.D., and Paradis, S. (2018). Rem2 stabilizes intrinsic excitability and spontaneous firing in visual circuits. eLife *7*.

Mrsic-Flogel, T.D., Hofer, S.B., Ohki, K., Reid, R.C., Bonhoeffer, T., and Hübener, M. (2007). Homeostatic regulation of eye-specific responses in visual cortex during ocular dominance plasticity. Neuron *54*, 961–972.

Nelson, S.B., and Valakh, V. (2015). Excitatory/Inhibitory Balance and Circuit Homeostasis in Autism Spectrum Disorders. Neuron *87*, 684–698.

Niell, C.M., and Stryker, M.P. (2008). Highly selective receptive fields in mouse visual cortex. J. Neurosci. *28*, 7520–7536.

O'Brien, W.T., and Klein, P.S. (2009). Validating GSK3 as an in vivo target of lithium action. Biochem. Soc. Trans. *37*, 1133–1138.

Orefice, L.L., Zimmerman, A.L., Chirila, A.M., Sleboda, S.J., Head, J.P., and Ginty, D.D. (2016). Peripheral Mechanosensory Neuron Dysfunction Underlies Tactile and Behavioral Deficits in Mouse Models of ASDs. Cell *166*, 299–313.

Peça, J., Feliciano, C., Ting, J.T., Wang, W., Wells, M.F., Venkatraman, T.N., Lascola, C.D., Fu, Z., and Feng, G. (2011). Shank3 mutant mice display autistic-like behaviours and striatal dysfunction. Nature *472*, 437–442.

Peixoto, R.T., Wang, W., Croney, D.M., Kozorovitskiy, Y., and Sabatini, B.L. (2016). Early hyperactivity and precocious maturation of corticostriatal circuits in Shank3B(-/-) mice. Nat. Neurosci. *19*, 716–724.

Pisanu, C., Melis, C., and Squassina, A. (2016). Lithium Pharmacogenetics: Where Do We Stand? Drug Dev. Res. *77*, 368–373.

Pratt, K.G., Watt, A.J., Griffith, L.C., Nelson, S.B., and Turrigiano, G.G. (2003). Activity-dependent remodeling of presynaptic inputs by postsynaptic expression of activated CaMKII. Neuron *39*, 269–281.

Rybakowski, J.K. (2011). Lithium in neuropsychiatry: a 2010 update. World J. Biol. Psychiatry *12*, 340–348.

Schmeisser, M.J., Ey, E., Wegener, S., Bockmann, J., Stempel, A.V., Kuebler, A., Janssen, A.L., Udvardi, P.T., Shiban, E., Spilker, C., et al. (2012). Autistic-like behaviours and hyperactivity in mice lacking ProSAP1/Shank2. Nature *486*, 256–260.

Schmitzer-Torbert, N., Jackson, J., Henze, D., Harris, K., and Redish, A.D. (2005). Quantitative measures of cluster quality for use in extracellular recordings. Neuroscience *131*, 1–11.

Serret, S., Thümmler, S., Dor, E., Vesperini, S., Santos, A., and Askenazy, F. (2015). Lithium as a rescue therapy for regression and catatonia features in two SHANK3 patients with autism spectrum disorder: case reports. BMC Psychiatry *15*, 107.

Smith, G.B., Heynen, A.J., and Bear, M.F. (2009). Bidirectional synaptic mechanisms of ocular dominance plasticity in visual cortex. Philos. Trans. R. Soc. Lond. B Biol. Sci. *364*, 357–367.

Soden, M.E., and Chen, L. (2010). Fragile X protein FMRP is required for homeostatic plasticity and regulation of synaptic strength by retinoic acid. J. Neurosci. *30*, 16910–16921.

Speed, H.E., Kouser, M., Xuan, Z., Reimers, J.M., Ochoa, C.F., Gupta, N., Liu, S., and Powell, C.M. (2015). Autism-Associated Insertion Mutation (InsG) of Shank3 Exon 21 Causes Impaired Synaptic Transmission and Behavioral Deficits. J. Neurosci. *35*, 9648–9665.

Torrado Pacheco, A., Tilden, E.I., Grutzner, S.M., Lane, B.J., Wu, Y., Hengen, K.B., Gjorgjieva, J., and Turrigiano, G.G. (2019). Rapid and Active Stabilization of Visual Cortical Firing Rates Across Light-Dark Transitions. PNAS *116*, 18068–18077.

Turrigiano, G.G. (2017). The dialectic of Hebb and homeostasis. Philos. Trans. R. Soc. Lond. B Biol. Sci. *372*.

Turrigiano, G.G., and Nelson, S.B. (2004). Homeostatic plasticity in the developing nervous system. Nat. Rev. Neurosci. *5*, 97–107.

Turrigiano, G.G., Leslie, K.R., Desai, N.S., Rutherford, L.C., and Nelson, S.B. (1998). Activity-dependent scaling of quantal amplitude in neocortical neurons. Nature *391*, 892–896.

Verpelli, C., Dvoretskova, E., Vicidomini, C., Rossi, F., Chiappalone, M., Schoen, M., Di Stefano, B., Mantegazza, R., Broccoli, V., Böckers, T.M., et al. (2011). Importance of Shank3 protein in regulating metabotropic glutamate receptor 5 (mGluR5) expression and signaling at synapses. J. Biol. Chem. *286*, 34839–34850.

Wagner, F.F., Bishop, J.A., Gale, J.P., Shi, X., Walk, M., Ketterman, J., Patnaik, D., Barker, D., Walpita, D., Campbell, A.J., et al. (2016). Inhibitors of Glycogen Synthase Kinase 3 with Exquisite Kinome-Wide Selectivity and Their Functional Effects. ACS Chem. Biol. *11*, 1952–1963.

Wang, X., McCoy, P.A., Rodriguiz, R.M., Pan, Y., Je, H.S., Roberts, A.C., Kim, C.J., Berrios, J., Colvin, J.S., Bousquet-Moore, D., et al. (2011). Synaptic dysfunction and abnormal behaviors in mice lacking major isoforms of Shank3. Hum. Mol. Genet. *20*, 3093–3108.

Wang, X., Bey, A.L., Katz, B.M., Badea, A., Kim, N., David, L.K., Duffney, L.J., Kumar, S., Mague, S.D., Hulbert, S.W., et al. (2016). Altered mGluR5-Homer scaffolds and corticostriatal connectivity in a Shank3 complete knockout model of autism. Nat. Commun. *7*, 11459.

Wang, W., Li, C., Chen, Q., van der Goes, M.S., Hawrot, J., Yao, A.Y., Gao, X., Lu, C., Zang, Y., Zhang, Q., et al. (2017). Striatopallidal dysfunction underlies repetitive behavior in Shank3-deficient model of autism. J. Clin. Invest. *127*, 1978–1990.

Yang, M., Bozdagi, O., Scattoni, M.L., Wöhr, M., Roullet, F.I., Katz, A.M., Abrams, D.N., Kalikhman, D., Simon, H., Woldeyohannes, L., et al. (2012). Reduced excitatory neurotransmission and mild autism-relevant phenotypes in adolescent Shank3 null mutant mice. J. Neurosci. *32*, 6525–6541.

Yi, F., Danko, T., Botelho, S.C., Patzke, C., Pak, C., Wernig, M., and Südhof, T.C. (2016). Autism-associated SHANK3 haploinsufficiency causes Ih channelopathy in human neurons. Science *352*, aaf2669.

Zhong, L.R., Chen, X., Park, E., Südhof, T.C., and Chen, L. (2018). Retinoic Acid Receptor RARα-Dependent Synaptic Signaling Mediates Homeostatic Synaptic Plasticity at the Inhibitory Synapses of Mouse Visual Cortex. J. Neurosci. *38*, 10454–10466.

Zhou, Y., Kaiser, T., Monteiro, P., Zhang, X., Van der Goes, M.S., Wang, D., Barak, B., Zeng, M., Li, C., Lu, C., et al. (2016). Mice with Shank3 Mutations Associated with ASD and Schizophrenia Display Both Shared and Distinct Defects. Neuron *89*, 147–162.

Zhou, Y., Sharma, J., Ke, Q., Landman, R., Yuan, J., Chen, H., Hayden, D.S., Fisher, J.W., 3rd, Jiang, M., Menegas, W., et al. (2019). Atypical behaviour and connectivity in SHANK3-mutant macaques. Nature *570*, 326–331.

Zhu, M., Idikuda, V.K., Wang, J., Wei, F., Kumar, V., Shah, N., Waite, C.B., Liu, Q., and Zhou, L. (2018). Shank3-deficient thalamocortical neurons show HCN channelopathy and alterations in intrinsic electrical properties. J. Physiol. *596*, 1259–1276.

STAR★METHODS

KEY RESOURCES TABLE

REAGENT or RESOURCE	SOURCE	IDENTIFIER
Antibodies		
Mouse monoclonal anti-GluA2 15F1	Eric Gouaux-OHSU	N/A
Guinea Pig anti-Shank3	Synaptic Systems	Synaptic Systems Cat# 162 304; RRID: AB_2619863
Guinea Pig anti-VGluT1	Synaptic Systems	Synaptic Systems Cat# 135 304; RRID: AB_887878
Rabbit anti-Shank3	Synaptic Systems	Synaptic Systems Cat# 162 302; RRID: AB_2619862
Chemicals, Peptides, and Recombinant Proteins		
GSK 3 Inhibitor (GSK3i) BRD0320	Florence Wagner-Broad Institute	N/A
Tetrodotoxin	Tocris	Catalogue # 1069 CAS no. 18660-81-6
Picrotoxin	Sigma	Catalogue # P1675 CAS no. 124-87-8
AP5	Tocris	Catalogue # 0105 CAS no. 76326-31-3
Critical Commercial Assays		
Lipofectamine 2000	Thermo Fisher	11668-027
Experimental Models: Organisms/Strains		
Rats: Long-Evans	Charles River Labs.	Strain code: 006
Mouse: Shank3B knockout mice (B6.129-Shank3tm2Gfng/J)	Jackson Laboratory	Stock No: 017688
Recombinant DNA		
Short Hairpin Insenstitve Shank3 (PDEST53)	Chiara Verpelli; Verpelli et al., 2011	N/A
Shank3 Short Hairpin (PVLTHM)	Chiara Verpelli; Verpelli et al., 2011	N/A
Software and Algorithms		
Igor Pro	Wavemetrics	https://www.wavemetrics.com/products/igorpro/igorpro.htm
MATLAB	Mathworks	https://www.mathworks.com/products/matlab.html
Python (Seaborn)	Python Software Foundation	https://seaborn.pydata.org
BORIS	Friard and Gamba, 2016	N/A
Metamorph	Molecular Devices	https://www.moleculardevices.com/products/cellular-imaging-systems/acquisition-and-analysis-software/metamorph-microscopy
Microsoft Excel	Microsoft	https://products.office.com/en-us/excel

LEAD CONTACT AND MATERIALS AVAILABILITY

Further information and requests for resources should be directed to and will be fulfilled by the Lead Contact, Dr. Gina Turrigiano (turrigiano@brandeis.edu).

This study did not generate new unique reagents.

EXPERIMENTAL MODEL AND SUBJECT DETAILS

The Brandeis University Institutional Animal Care and Use Committee approved all procedures, which conformed to the National Institutes of Health Guide for the Care and Use of Laboratory Animals. For all experiments, mice or rats of both sexes were used; no differences were noted between males and females and data were combined. For the Shank3b mouse (Peça et al., 2011) founder mice were obtained from Jackson labs (Stock No: 017688). Genotyping was done based on primers as previously described (Peça et al., 2011). Long-Evans rats were obtained from Charles River, Wilmington MA. Ages for different experiments (*in vitro* and *in vivo*) are given below.

METHOD DETAILS

Primary cortical neuron culture

Dissociated cultures were prepared from the visual cortex of postnatal day 1 (P1)–P3 Long-Evans rat pups, or WT or KO Shank3b littermate mice, and plated onto a layer of confluent astrocytes on glass-bottom dishes as described previously (Pratt et al., 2003). All experiments were performed after 7-11 days *in vitro (*DIV). All experiments on cultured neurons were performed on neurons with a pyramidal morphology as described (Pratt et al., 2003). All transfections were carried out using Lipofectamine 2000 (Thermo Fisher). Transfected neurons were identified by GFP fluorescence. All control and treatment conditions were run in parallel on sister cultures to minimize variation from individual culture preps and were repeated on a minimum of 3 independent cultures.

Immunocytochemistry and Image analysis

Neurons were transfected on DIV 6-9 for 2-2.5 days with Lipofectamine 2000, and treated with 5 uM TTX or 100 μM PTX for 24 hr prior to fixation in 3.7% PFA/5% sucrose. Surface GluA2 immunolabeling was performed under non-permeabilizing conditions and all other immunolabeling was performed under permeabilizing conditions with 0.25% Triton X-100. Primary antibodies included Shank3 α gp (Synaptic Systems 162 304), Shank3 α rab (1:400) (162 302Synaptic Systems), Vglut1 (1:500) (catalog no. 135 304, Synaptic Systems), GluA2 (1:1000) α ms (gift from Gouaux lab, OHSU). Immunostained neurons were coverslipped and imaged on a Leica SP5 or Zeiss 880 confocal microscope. Digital images were analyzed in Metamorph (Molecular Devices). For ROI analysis of total intensity, dendritic ROI's were drawn by hand and background subtracted using an ROI without neurons. Punctate Shank3 or other signals from synaptic markers was identified using the Granularity function in Metamorph. Granules present in both channels were identified as colocalized (a minimum of 3 pixel overlap) and intensities were quantified as previously described (Gainey et al., 2009). Dendritic regions on the apical-like dendrites were analyzed to ensure uniformity in comparisons across neurons.

Culture Electrophysiology

recordings were performed in whole cell voltage clamp at room temperature; holding potential was −70 mV. Neurons with pyramidal morphology were targeted by visual inspection. Bath solution was ACSF containing (in mM): 126 NaCl, 5.5 KCl, 2 MgSO4, 1 NaH2PO4, 25 NaHCO3, 2 CaCl2, 14 dextrose; and 25 uM picrotoxin, 25 uM D-amino-5-phosphovaleric acid (AP5), and 0.1 μM TTX to isolate AMPA-mediated mEPSCs. Internal solution composition (in mM) was: 120 $KMeSO_4$, 10 KCl, 2 $MgSO_4$, 10 K-HEPES, 0.5 EGTA, 3 K_2ATP, 0.3 NaGTP, and 10 Na_2phosphocreatine. Dextrose was added to adjust osmolarity to 320-330 mOsm. Neurons were excluded from analysis if resting membrane potential (Vm) was > −55 mV, series resistance (Rs) was > 20 MΩ, input resistance (Rin) was < 100 MΩ, Rin or Vm changed by > 30%, or < 25 mEPSCs were obtained. MEPSCs were detected and analyzed using in-house software; detection criteria included amplitudes > 5 pA and rise times < 3 ms. To construct cumulative histograms the first 25 events for each neuron were included. For *f-I* curves transfected neurons were recorded in ACSF with 25 uM Picrotoxin, 50 uM AP5 and 25 uM DNQX. Cells were recorded in whole cell configuration in current clamp and a series of depolarizing step ranging from 30 pA to 250 pA were delivered. Data from EV transfected cells and untransfected control cells were not different and were pooled for some experiments. *f-I* recordings were analyzed using custom software written in-house in IGOR pro or MATLAB. All mEPSC and *f-I* data were analyzed blind to condition.

Slice Electrophysiology

Coronal brain slices containing V1 were prepared as described (Hengen et al., 2013). Monocular V1 (V1m) was identified, and whole-cell patch-clamp recordings were obtained from layer 2/3 pyramidal neurons, as previously described (Hengen et al., 2013). V1m was identified using the shape and morphology of the white matter as a reference. Neurons were visualized with a 40x water-immersion objective using infrared-differential interference contrast optics. Internal recording solution contained (in mM) 115 Cs-Methanesulfonate, 10 HEPES(Fisher), 10 BAPTA 4Cs(Fisher), 5.37 Biocytin(Invitrogen), 2 QX-314 Cl(Tocris), 1.5 MgCl2, 1 EGTA, 10 Na2-Phosphocreatine, 4 ATP-Mg, 0.3 GTP-Na, with sucrose added to bring osmolality to 295, and CsOH added to bring pH to 7.35. For mEPSC recordings, neurons were voltage clamped to −70 mV in standard ACSF containing TTX (0.2 uM), APV (50 uM), and picrotoxin (25 uM), continuously oxygenated and warmed to 34°C. Neurons were excluded from analysis if series resistance was > 20 MΩ or if input resistance was < 80 MΩ. Pyramidal neurons were identified and targeted by the presence of an apical dendrite and teardrop shaped soma, and morphology was confirmed by post hoc reconstruction of biocytin fills.

Reagents

GSK3i (BRD0320-Broad Institute), LiCl2 (Sigma), TTX (Tocris), PTX (Sigma), DNQX (Sigma), AP5 (Tocris), DMSO (Sigma), Alexa 488, 555, 647 (Invitrogen).

DNA constructs

Shank3 SH and Rescue plasmids were obtained from Dr. Chiara Verpelli and were previously characterized (Verpelli et al., 2011).

Surgery and *in vivo* recordings

Electrode array implantations were carried out on littermate Shank3 and WT mice generated from Het-Het matings (WT: n = 7, KO: n = 7; P21-24 at time of surgery). Mice were implanted unilaterally under isofluorane anesthesia with custom 16-channel 33 μm tungsten microelectrode arrays (Tucker-Davis Technologies, Alachua, FL, wire diameter 33 μm, electrode spacing 250 μm, row separation 375 μm, tip angle 45°) into V1. Wires were cut to different lengths so as to span all layers of V1. Surgical procedure was as described previously (Hengen et al., 2013). Briefly, the skull was exposed and cleaned and two holes were drilled above the cerebellum and right hemisphere to support stainless steel miniature screws. After drilling a craniotomy, the electrode array was inserted in V1 in the left hemisphere to a depth of 1.0 mm for the longest wire and grounded to both screws. Dental cement was used to connect the array to the entirety of the exposed bone surface as well as the steel screws. The total headcap weight was less than 0.8 g.

Animals were allowed to recover for two full days post-surgery in transparent plastic cages with *ad libitum* access to food and water. Recording began on the third day after surgery. Animals were allowed to habituate to the recording chamber for ~12 hours prior to the start of the experiment. The recording chamber (12''x12,'' plexiglass) was lined with 1.5'' of bedding and housed two littermates (one Shank3 KO and one WT mouse). Animals had *ad libitum* food and water and were separated by a clear plastic divider with several holes allowing for tactile and olfactory interaction but preventing jostling of headcaps and electrode arrays. Novel toys were introduced every 24h, to enrich the animals' experience and promote activity and exploration. Lighting and temperature were kept constant (LD 12:12, lights on at 7:30 am, 21°C, humidity 25%–55%).

Data were collected continuously for nine days (~200 hours). After lights off on the third day of baseline recording animals were removed from the recording chamber and placed under isoflurane anesthesia. The eyelid contralateral to the implanted hemisphere was sutured. The procedure lasted ~15 min per animal. Mice were fully recovered from anesthesia ~15 minutes after re-introduction in the recording chamber. The lid suture was kept in place for 6 days. Electrode placement was verified histologically at the end of each experiment and only recordings from V1m were included.

Histology

At the end of each *in vivo* recording experiment, animals were administered a lethal dose of ketamine/xylazine (dosage: 200 mg/kg and 7 mg/kg respectively) and transcardially perfused with 0.9% saline followed by 4% paraformaldehyde. Brains were postfixed in 10% formalin and 30% sucrose solution for > 3 days. Brains were then sectioned at 60 μm, mounted on glass slides, stained using cresyl violet according to a standard Nissl staining protocol, and imaged using a light microscope. Electrode tracks were visually identified in stained sections. Data from electrodes that were not in V1 were excluded from analyses.

In vivo data analysis

Voltage signals were collected at 25 kHz and streamed to disk using a Tucker-Davis Technologies Neurophysiology Workstation and Data Streamer. Spike extraction was performed offline using custom software (MATLAB). Briefly, a 500 kHz high-pass filter was applied and threshold crossings (threshold: −4 standard deviations from the mean signal) were detected and saved (8 samples before and 24 samples after the crossing). Spike waveforms were re-sampled at 3x the original sampling rate, then subjected to principal component analysis (PCA) and the first four principal components were used to cluster each channel's waveforms using the KlustaKwik algorithm (Harris et al., 2000). Clusters were not cut manually; instead, they were merged or trimmed as described previously (Hengen et al., 2016).

Spike sorting was performed using custom software (MATLAB) that relies on a machine learning approach, as described previously (Torrado Pacheco et al., 2019). For each cluster, a set of 19 features was extracted, including ISI contamination (percentage of ISIs < 3 ms), similarity to regular spiking unit (RSU) and fast-spiking (FS) waveform templates, 60 Hz noise contamination, rise and decay time and slope of the mean waveform, and waveform amplitude and width. Cluster quality was also ensured by thresholding of L-Ratio and Mahalanobis distance (Schmitzer-Torbert et al., 2005). The set of resulting features was fed to a random forest classifier, trained on a set of 1200 clusters scored by human experts (ATP and KBH). Each cluster was assigned a quality value between 1 and 4, with 1 and 2 representing single-unit data. Each cluster also had a confidence score for its classification, ranging from 0% to 100%. Only units with quality 1 or 2 were used for analysis. Clusters with quality 2 and a confidence score less than 70% were excluded. Only regular spiking (putative pyramidal) units (RSUs) were used for analysis. Cells were classified into RSUs or fast spiking units (FSUs) based on the following mean waveform parameters: time between the negative peak and the first subsequent positive peak (trough-to-peak time); slope of the waveform from 0.4 msec after the negative peak to last sample (tail slope). RSUs were identified as having a tail slope > 0.005 and trough-to-peak time > 0.39 msec (Niell and Stryker, 2008); only RSUs were included.

Recordings were time-stamped so that time 0 represents 7:30 am (lights on) on the first baseline day. The recording was split into nine 24-hour periods starting at this time. The set of spikes from each period was fed to the clustering and spike-sorting algorithm. The majority of cells could not be followed continuously over these 9 day experiments, so instead we compared the ensemble averages and distributions for all RSUs detected for each day. The criteria used to determine when a cell was on- or offline were as described previously(Hengen et al., 2016); to obtain reasonable estimates of mean firing rates only neurons recorded for > 2 hours were included.

Intrinsic Signal Imaging

All imaging experiments were performed as previously described (Moore et al., 2018). In brief, animals between the ages of P25-P26 were used for lid suturing. The Ocular Dominance of animals was either measured at 3 days (P28-P29) or 6 days (P31-32) of deprivation after lid suture, and colony mates (either Shank3b$^{+/+}$ or $^{-/-}$) were used for imaging. At the beginning of the experiment, animals were anesthetized by isoflurane in an anesthesia chamber at 2.5%–3.0% at 150mL/min using a SomnoSuite (Kent Scientific). Animals were maintained from 1.0%–2.0% anesthesia throughout surgical procedures. A single dose of chlorprothixene at 10mg/kg was given to the animal before proceeding. If animals were previously sutured, sutures were gently removed and both eyes had eye ointment applied to them. The scalp was then opened and skull exposed, where tissue was cleared and a small headpost was affixed to the skull on the opposing side of the imaging site using an adhesive (ZAP Gel, Pacer Technologies). The skull was thinned in the desired imaging area using a scalpel, 2% agarose was applied to the thinned area and a coverslip was added on top and adhered with cyanoacrylate glue. During imaging, anesthesia was reduced to 0.4%–1.0% and mice were shown 20 repetitions of drifting grating stimuli at 0 or 90 degrees, 100% contrast, 2Hz temporal frequency, 0.05 cpd, lasting for 5 s with an interstimulus interval of 15 s, including a blank, gray screen as a control stimulus. A red light at 675 nm was shown over the window to detect changes in reflectance as stimuli were played. Each eye was alternately shown the same set of stimuli and the eye not being stimulated was blocked with a flexible, light-blocking material. Data analysis was performed as described (Moore et al., 2018) using MATLAB scripts written in house (https://github.com/VH-Lab/vhlab_vhtools/). Animals were excluded from analysis if the brain appeared damaged or was unresponsive to visual stimulation.

Grooming behavior assay

Grooming was quantified from Shank3 KO and WT littermate pairs between 6-8 weeks of age, as described previously (Peça et al., 2011). Animals were video recorded using cage-mounted cameras and Debut video capture software. Recordings were performed in the homecage using custom-made clear dividers (with holes so the mice could interact through touch and smell) to separate WT from KO littermates. Animals were allowed to habituate to the divided cage for several hours before self-grooming behavior (minutes spent grooming) was quantified for a 3 hr period spanning lights on (1.5 hr at end of dark phase, 1.5 hr at beginning of light phase). For each pair we first obtained a baseline measurement for each animal, and then quantified self-grooming again after 1 week of lithium treatment. The lithium treatment followed published protocols (Gideons et al., 2017) and consisted of maintaining animals on 0.2% LiCl chow for 7 days; animals were provided with 0.9% NaCl saline and water ad libidum to control for ion imbalances known to occur with Li treatment. Data were manually scored for spontaneous grooming behaviors, using Behavioral Observation Research Interactive Software (BORIS; Gamba, 2016). The number of bouts were noted as well as the length of each bout. Self-grooming included forepaw grooming of the head, ears, paws, back, and tail, and licking or scratching of limbs or other bodily surfaces using both the forepaws and hind legs (Kalueff et al., 2007; Peça et al., 2011).

QUANTIFICATION AND STATISTICAL ANALYSIS

The statistical test(s) used for each dataset are indicated in Table S1. For comparison of two groups two tailed t test were used as described. Comparison among multiple groups was via ANOVA in conjunction with Levene's test for homogeneity. This was followed by post hoc tests adjusted for multiple comparisons with Bonferroni's correction as noted. Comparison of multiple non-normally distributed groups was via the Kruskal-Wallis test, followed by pairwise Wilcoxon rank-sum tests adjusted for multiple comparisons using the Benjamini-Hochberg procedure (false discovery rate = 0.05). Comparison of cumulative distributions was done with Kruskal–Wallis test or Anderson-Darling test followed by either Bonferroni's correction or Benjamini-Hochberg FDR procedure (FDR = 0.05). P values below 0.05 were considered significant. The actual p values of each comparison conducted are given in Table S1.

DATA AND CODE AVAILABLITY

The published article includes all data generated during this study. The raw electrophysiology data supporting the current study have not been deposited in a public repository because there is currently no standardized format or repository for such data, but they are available from the corresponding author on request.